On the electronic structures of gaseous transition metal halide complexes, FeX_4^- and MX_3^- (M=Mn, Fe, Co, Ni, X=Cl, Br), using photoelectron spectroscopy and density functional calculations

Xin Yang, Xue-Bin Wang, and Lai-Sheng Wang[a)]
Department of Physics, Washington State University, Richland, Washington 99352, and W.R. Wiley Environmental Molecular Sciences Laboratory, MS K8-88, Pacific Northwest National Laboratory, Richland, Washington 99352

Shuqiang Niu and Toshiko Ichiye
School of Molecular Biosciences, Washington State University, Pullman, Washington 99164-4660, and Department of Chemistry, Georgetown University, Washington, DC 20057-1227

(Received 5 June 2003; accepted 28 July 2003)

We report a photoelectron spectroscopy (PES) and theoretical study on a series of transition metal halide complexes: FeX_4^- and MX_3^- (M=Mn, Fe, Co, Ni, X=Cl, Br). PES spectra were obtained at two photon energies (193 and 157 nm), revealing the complicated electronic structures of these metal complexes and their variation with the ligand-field geometry and metal center substitution. Density functional calculations were carried out to obtain information about the structures, energetics, and molecular orbitals of the metal complexes and used to interpret the PES spectra. For the tetrahedrally coordinated ferric complexes (FeX_4^-), the PES data directly confirm the ''inverted level scheme'' electronic structure, where the Fe $3d$ electrons lie below those of the ligands due to a strong spin-polarization of the Fe $3d$ levels. For the three-coordinate complexes (MX_3^-), the calculations also revealed strong spin polarizations, but the molecular orbital diagrams present a ''mixed level scheme,'' in which the ligand orbitals and the Fe $3d$ majority spin orbitals are spaced closely in the same energy regions. This ''mixed level scheme'' is due to the larger splitting of the $3d$ orbitals in the stronger D_{3h} ligand field and the smaller spin polarizations of the divalent metal centers. The calculations show that the metal $3d$ orbitals are stabilized gradually relative to the ligand orbitals from Mn to Ni in the tri-halide complexes consistent with the PES spectral patterns.
 [DOI: 10.1063/1.1610431]

I. INTRODUCTION

High spin Fe centers play important roles in many metalloproteins, particularly in iron–sulfur proteins. Extensive theoretical[1–8] and spectroscopic[9–18] studies have been carried out to investigate the electronic structures of Fe complexes. For a high spin Fe center in the presence of a weak ligand field, such as thiolate, calculations indicate that strong exchange interactions split the Fe $3d$ levels into a set of spin-up (α) and a set of spin-down (β) levels. The majority spin levels (α) are considerably stabilized in energy with the primarily ligand-based levels in between the Fe $3d$ minority and majority levels, resulting in the so-called ''inverted level scheme.'' [3–7] Thus in the high spin ferric complexes, the highest occupied molecular orbital (HOMO) becomes primarily ligand-based orbitals. This ''inverted level scheme'' has been confirmed by photoelectron and x-ray absorption spectroscopy experiments for the ferric complexes such as $Fe^{III}(SR)_4^-$ and $Fe^{III}Cl_4^-$.[14–18] However, the energy level schemes of ferrous compounds are more complicated and remain controversial. For iron–sulfur systems, theoretical calculations showed that the differences in the orbital energy diagrams between the ferric and ferrous complexes are minor. The presence of the extra electron in the ferrous complexes has only a small effect on the orbital energies, aside from a uniform upward shift.[3,5] But single-crystal spectroscopic studies on $Fe^{II}(SR)_4^{2-}$ [$R=2-(Ph)C_6H_4$] suggested a picture consistent with the standard spin-restricted ligand field model and indicated a large electronic relaxation upon reduction.[13] A theoretical and photoelectron spectroscopic study on the ferrous $Fe^{II}Cl_4^{2-}$ complex also indicated that it is consistent with the normal level scheme, but with a significant spin-polarization.[15]

While most research focused on the tetrahedral coordinate systems, three-coordinate ferrous complexes have also aroused much interest as models for the trigonal sites of the $MoFe_7S_9$ cofactor of nitrogenase,[19] although a recent x-ray structure suggests that the Fe may be coordinated additionally by a nitrogen atom.[20] *Q*-band ENDOR[21] and Mössbauer[22] data suggest that the majority of the trigonal sites are high-spin ferrous centers exhibiting a slightly distorted planar geometry with idealized C_{3h} symmetry. Model complexes, such as $Fe(SR_3)^-$ ($R=C_6H_2$-2,4,6-tBu$_3$)[23,24] and $[LFe^{II}X]^0$ (L=β-diketiminate; X=Cl^-, CH_3^-, $NHTol^-$, $NHtBu^-$)[25] have been synthesized and studied by Mössbauer and electron paramagnetic resonance experiments. However, there has been no experimental work on

a)Author to whom all correspondence should be addressed. Electronic mail: ls.wang@pnl.gov

gaseous $M^{II}L_3^-$ complexes to our knowledge.

Gas-phase photodetachment photoelectron spectroscopy (PES) is a powerful tool to probe the electronic structure and chemical bonding of isolated molecules or inorganic complexes without the perturbation present in the condense phase. We have developed an experimental technique, which couples electrospray ionization (ESI) with PES, to study solution phase species in the gas phase.[26] ESI is a versatile technique, allowing ionic species in solution samples to be transported into the gas phase. Our recent research has shown that the ESI-PES technique is ideal for investigating multiply charged anions in the gas phase,[27] as well as anionic metal-complexes commonly present in solution.[28–31] Using this technique, we have reported a preliminary study of a series of [1Fe]-complex anions involved in the Fe^{II}/Fe^{III} redox couple, with emphasis on the determination of the intramolecular reorganization energies.[30] Systematic PES and theoretical studies on a series of ferric complexes, $Fe^{III}(SCH_3)_4^-$, $Fe^{III}(SCN)_4^-$, $Fe^{III}(S_2\text{-o-xyl})_2^-$, and tetracoordinated, $Fe^{II}(S_2\text{-o-xyl}))_2^{2-}$ and $Fe^{II}(SCN)_4^{2-}$, and tricoordinated, $Fe^{II}(SCH_3)_3^-$ and $Fe^{II}(SCN)_3^-$, ferrous complexes have been carried out recently.[32,33] The spectral patterns of these complexes agree well with spin-polarized calculations, which suggest that the ''inverted level scheme'' is a general feature of the electronic structures of these Fe–S complexes although they have different oxidation states and coordination numbers.

In the current paper, we extend the PES and theoretical studies to a series of transition metal halide complexes, FeX_4^- and MX_3^- (M=Mn, Fe, Co, Ni, X=Cl, Br). Electronic structures of these complexes and their systematic variation upon changes of the ligand-field geometry and the metal centers are investigated. The PES spectra of the tetrahedrally coordinated ferric complexes FeX_4^- (X=Cl, Br) were obtained at 157 nm. Density functional theory (DFT) calculations were carried out to help interpret the PES data. All the spectral features were assigned to detachment from ligand orbitals by comparing with the spectra of d^0 complexes, ScX_4^- (X=Cl, Br), confirming that the electronic structure of FeX_4^- (X=Cl, Br) conforms to the ''inverted level scheme.'' The PES spectra of the series of tricoordinated $3d$ transition metal complexes were taken at two photon energies: 193 and 157 nm. The spectral features show strong ligand and photon energy dependence. DFT calculations were carried out for all the tri-coordinate complexes and revealed strong spin polarizations. But the molecular orbital (MO) diagrams present a ''mixed level scheme'' for the tri-coordinate complexes, in which the ligand-based MOs and the $3d$ majority spin orbitals are spaced closely in the same energy regions. This ''mixed level scheme'' is consistent with the PES spectral pattern.

II. EXPERIMENTAL AND COMPUTATIONAL METHODS

The experiment was carried out with the ESI-PES apparatus, which has been described in detail elsewhere.[26] Only a brief description of the experimental procedure is given here. To produce the desired anions, we used 10^{-3} molar solutions of $M^{III}X_3$ (M=Fe, Sc; X=Cl, Br), $M^{II}X_2$ (M=Fe, Ni), and $(NEt_4)_2M^{II}X_4$ (M=Mn, Co), respectively, in a water/methanol (1:5 ratio) mixed solvent. The sample solutions were sprayed through a 0.01-mm-diam syringe needle biased at −2.2 kV in ambient atmosphere. Negatively charged ions emerging from a desolvation capillary were guided by a radio frequency-only quadrupole ion-guide into an ion trap, where the ions were accumulated for 0.1 s before being pushed into the extraction zone of a time-of-flight mass spectrometer. The solutions of the M^{III} samples primarily yielded the MX_4^- anions, whereas those of the M^{II} samples gave mainly the MX_3^- complexes. No doubly charged $M^{II}X_4^{2-}$ complexes were observed because they were no expected to be stable in the gas phase.[34]

In the PES experiment, the MX_4^- and MX_3^- anions of interest were mass-selected and decelerated before being intercepted by a laser beam in the detachment zone of the magnetic-bottle photoelectron analyzer. For the current study, two photon energies, 193 nm (6.424 eV) and 157 nm (7.866 eV), from an excimer laser were used for photodetachment. The photoelectrons were collected at nearly 100% efficiency by the magnetic-bottle and analyzed in a 4-m-long time-of-flight tube. Photoelectron time-of-flight spectra were collected and then converted to kinetic energy spectra, calibrated by the known spectra of I^- and O^-. The binding energy spectra were obtained by subtracting the kinetic energy spectra from the corresponding photon energies. The energy resolution was about 10 meV (full width at half maximum) for ~0.5 eV electrons, as measured from the spectrum of I^- at 355 nm.

The broken-symmetry DFT method,[5–7,35] specifically with Becke's three parameter hybrid exchange functional[36,37] and the Lee–Yang–Parr correlation functional (B3LYP),[38] was used for geometry optimization and for the investigation of the electronic structure and energetics of the complexes. Our previous work showed that the B3LYP method gives a reliable description of the structural and redox properties of iron–sulfur clusters with respect to other conventional *ab initio* and DFT methods.[33,39] A set of triple-ζ basis sets, 6-311++G($3df$,$3pd$),[40–42] were employed for all atoms in the calculations. The triple-ζ basis sets (611111111/51111/311) were enhanced with three sets of f functions and one set of g function for the Mn, Fe, Co, and Ni atoms. No symmetry restraints were imposed during geometry optimizations. Because all the FeX_4^- and MX_3^- species are weak field ligand complexes, their reduced and oxidized species usually have high-spin ground states. Although there is a small amount of spin delocalization between the metal center and ligands, the calculated S^2 values $\{S^2=S(S+1)\}$ show that spin contamination problems do not significantly affect the DFT results of these high-spin states. The MO analysis is on the basis of Kohn–Sham orbitals, which are a good basis for qualitative interpretation of MOs.[43]

All calculations were performed using the NWCHEM[44] program package. The molecular orbital visualizations were performed using the extensible computational chemistry environment (Ecce) application software.[45]

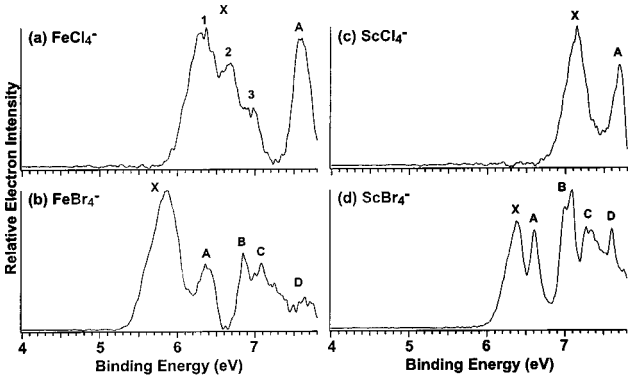

FIG. 1. Photoelectron spectra of (a) $FeCl_4^-$, (b) $FeBr_4^-$, (c) $ScCl_4^-$, and (d) $ScBr_4^-$ at 157 nm (7.866 eV).

III. EXPERIMENTAL RESULTS

A. FeX_4^- and ScX_4^- (X=Cl, Br)

Figure 1 shows the PES spectra of $FeCl_4^-$ and $FeBr_4^-$, compared with those of $ScCl_4^-$ and $ScBr_4^-$, which formally have no $3d$ electrons on the metal center. Two well-separated bands (X,A) were observed in the spectrum of $FeCl_4^-$ [Fig. 1(a)]. The band X was very broad with three discernible fine features (1, 2, 3). The band A was relatively sharp and appeared to be cut off. The spectrum of $FeBr_4^-$ showed more spectral features (labeled from X to D) because of its lower electron binding energies and larger spin–orbit splitting.

The scandium tetrahalide anions are superhalogens[46] and exhibit extremely high electron binding energies. The overall spectral patterns and shifts of $ScCl_4^-$ [Fig. 1(c)] and $ScBr_4^-$ [Fig. 1(d)] are similar to those of $FeCl_4^-$ and $FeBr_4^-$, respectively, except for the broad widths of the X bands in the spectra of the Fe halide complexes. The A band in the spectrum of $ScCl_4^-$ also appeared to be cut off.

B. FeX_3^- and MnX_3^- (X=Cl, Br)

The spectra of FeX_3^- and MnX_3^- (X=Cl, Br) are shown in Fig. 2 at 193 and 157 nm. The spectra of the two ferrous complexes exhibit a well-resolved and relatively weak threshold peak (X). The very weak feature near 3.6 eV in the 193 nm spectrum of $FeCl_3^-$ [Fig. 2(e)] was due to Cl^- as a result of photodissociation $(FeCl_3^- \rightarrow FeCl_2 + Cl^-)$, which appeared to occur only for this complex at 193 nm. The spectra of the two ferrous halides are similar, in particular the X band in both species has nearly the same binding energy. However, more features were observed in the bromide complex [Fig. 2(b)] and they shifted to lower binding energies, analogous to that observed in the ferric halides [Figs. 1(a) and 1(b)]. It should also be pointed out that the B band in the spectra of $FeBr_3^-$ seemed to show a strong photon-energy dependence: its relative intensity was significantly reduced in the 157 nm [Fig. 2(b)] compared to the 193 nm spectrum [Fig. 2(f)].

The spectral patterns of MnX_3^- are very similar to those of the FeX_3^- counterpart. There is almost a one-to-one correspondence between the spectral features of the Fe and Mn complexes as labeled in Fig. 2, except for the absence of the

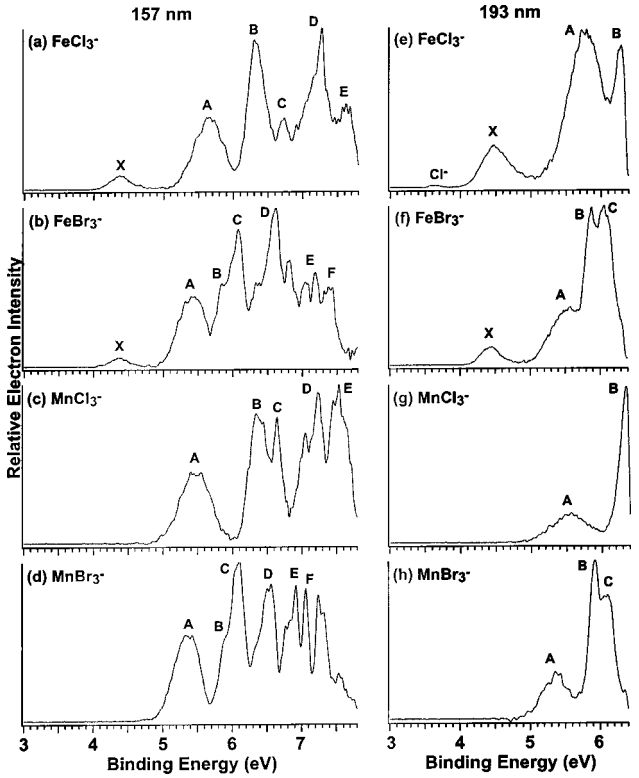

FIG. 2. Photoelectron spectra of $FeCl_3^-$, $FeBr_3^-$, $MnCl_3^-$, and $MnBr_3^-$ at 157 and 193 nm (6.424 eV).

X feature in the spectra of the Mn complexes. The photon energy dependence of the B band for the ferrous bromide was also observed for the Mn bromide. In addition, we also observed a strong photon energy dependence of the B band in the spectra of Mn chloride: the relative intensity of the B band was significantly reduced in the 157 nm [Fig. 2(c)], similar to that observed in the bromide complex. A similar phenomenon could not be observed in the ferrous chloride because its B band has too high a binding energy and was partly cut off in the 193 nm [Fig. 2(e)].

C. CoX_3^- and NiX_3^- (X=Cl, Br)

Figure 3 shows the spectra of CoX_3^- and NiX_3^- (X=Cl, Br) at 193 and 157 nm. The spectral features become considerably more congested for these species, especially for the Ni complexes. The spectra likely contain numerous overlapping features and only some of them are tentatively labeled for later discussion. The spectra of $CoCl_3^-$ are quite similar to those of $FeCl_3^-$ except near the threshold region: the higher binding energy bands $(A-E)$ are similar in their relative intensities and occur in the same energy range in both systems. However, whereas a single weak threshold band (X) was observed for $FeCl_3^-$ which is well separated from the A bands, two weak threshold bands $(X1, X2)$ seemed to be present for $CoCl_3^-$ [Fig. 3(a)] and were shifted to higher binding energies relative to the X band of $FeCl_3^-$. In addition, the $X2$ band of $CoCl_3^-$ showed a strong photon energy dependence, being much enhanced in the 193 nm spectrum [Fig. 3(e)]. The spectra of $CoBr_3^-$ were much more congested. Two threshold features $(X1, X2)$ can be tenta-

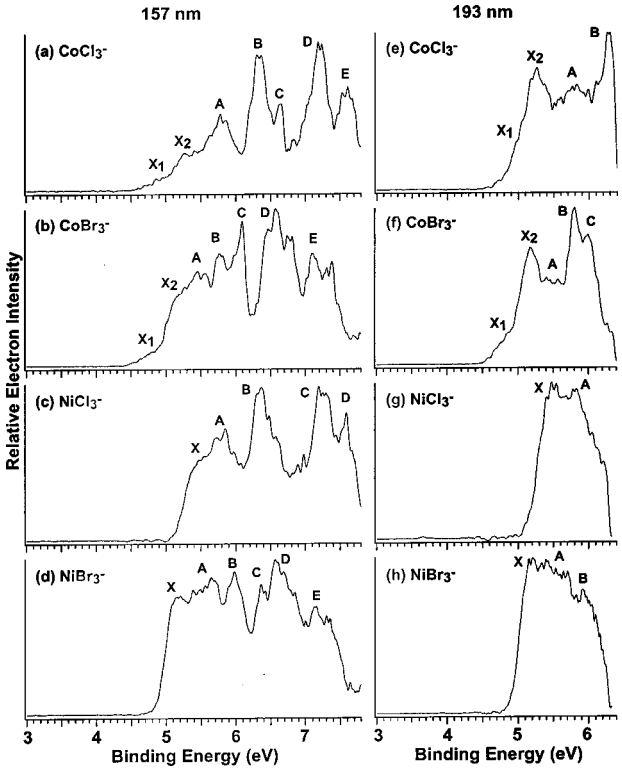

FIG. 3. Photoelectron spectra of $CoCl_3^-$, $CoBr_3^-$, $NiCl_3^-$, and $NiBr_3^-$ at 157 and 193 nm.

tively identified, which occur in the same binding energies as those in the $CoCl_3^-$ spectra, but the $X2$ component was overlapped with the A band [Fig. 3(b)].

The spectra of the two Ni halides were much more congested. The weak low binding energy features present in the spectra of the Fe and Co halides were not observed in the spectra of NiX_3^-. In addition, the threshold feature (X) in $NiBr_3^-$ was observed to shift to lower binding energies relative to that in $NiCl_3^-$, whereas in the Fe and Co halides the threshold peak was insensitive to the ligand.

D. Electron detachment energies

The adiabatic (ADE) and vertical (VDE) detachment energies of the threshold peaks of each complex are listed in Table I. The VDEs of all observed features are given in Table II. The ADE of the threshold peak represents the electron affinity of the neutral species. Because of the lack of vibrational resolution, it was determined approximately by drawing a straight line along the leading edge of the threshold band and then adding the instrumental resolution at that energy to the intersection with the binding energy axis. The VDE of each peak was measured directly from the peak maximum. The ADEs determined from the 193 and 157 nm spectra for the MX_3^- complexes were consistent, but the values from the 193 nm data are given in Table I because of the better resolution in the lower photon-energy spectra.

IV. THEORETICAL RESULTS

To understand the PES features of the $M^{III}X_4^-$ and $M^{II}X_3^-$ complexes and their variation with ligand types and the nature of the metal center and elucidate their electronic structures, we carried out a theoretical investigation using DFT method. The electronic structures of the complexes were qualitatively analyzed through molecular orbital theory.

A. FeX_4^- (X=Cl, Br) and the inverted level scheme

The tetra-coordinated ferric complexes, $Fe^{III}X_4^-$ (X = Cl, Br), were found to have T_d symmetry. Electron detachment results in a geometrical distortion from T_d to C_{2v}, where two *trans* $\angle$X–Fe–X angles increase by about 15° and the metal–ligand bond length decreases by about 0.1 Å. The spin-exchange interaction leads to strong spin polarization, splitting the occupied Fe $3d$ α-spin orbitals and β-spin orbitals. Most Cl($3p$)/Br($4p$) orbitals lie below the metal β-spin orbitals (unoccupied in the ferric complexes) and above the metal α-spin orbitals, resulting in the inverted level scheme, as shown in Fig. 4. The highest occupied MOs (HOMOs) of $Fe^{III}X_4^-$ are the degenerate Cl($3p$)/Br($4p$)

TABLE I. Measured and calculated adiabatic detachment energies (ADEs), vertical detachment energies (VDEs), and relaxation energies (λ_{oxd}) in eV of the threshold peaks of MX_4^- and MX_3^-.[a]

	ADE		VDE		λ_{oxd}	
	Expt.	Calc.	Expt.	Calc.	Expt.	Calc.
$Fe^{III}Cl_4^-$	6.00 (8)	5.65	6.32 (8)	6.02	0.32	0.37
$Fe^{III}Br_4^-$	5.50 (8)	5.37	5.85 (8)	5.63	0.35	0.26
$Sc^{III}Cl_4^-$	6.89 (8)	5.96	7.15 (8)	6.31	0.26	0.35
$Sc^{III}Br_4^-$	6.13 (8)	5.75	6.38 (8)	5.78	0.25	0.03
$Mn^{II}Cl_3^-$	5.07 (6)	4.44	5.50 (6)	4.98	0.43	0.54
$Mn^{II}Br_3^-$	5.03 (6)	4.54	5.36 (6)	4.91	0.33	0.37
$Fe^{II}Cl_3^-$	4.22 (6)	4.11	4.46 (8)	4.33	0.24	0.22
$Fe^{II}Br_3^-$	4.26 (6)	4.17	4.42 (6)	4.35	0.16	0.18
$Co^{II}Cl_3^-$	4.7 (1)	4.25	4.9 (1)	4.53	0.2	0.28
$Co^{II}Br_3^-$	4.6 (1)	4.25	4.8 (1)	4.49	0.2	0.24
$Ni^{II}Cl_3^-$	5.20 (8)	4.90	5.5 (1)	5.15	0.3	0.25
$Ni^{II}Br_3^-$	4.94 (8)	4.50	5.1 (1)	4.69	0.2	0.19

[a]The numbers in parentheses represent the uncertainties in the last digit. λ_{oxd} is defined as (VDE-ADE) (see Ref. 30).

TABLE II. Measured vertical detachment energies (VDEs), in eV for all observed features for MX_4^- and MX_3^-.[a]

	X	*A*	*B*	*C*	*D*	*E*	*F*
$Fe^{III}Cl_4^-$	6.32 (8)	7.58 (8)					
	6.67 (8)						
	6.97 (8)						
$Fe^{III}Br_4^-$	5.85 (8)	6.38 (8)	6.84 (8)	7.07 (8)	7.64 (8)		
$Sc^{III}Cl_4^-$	7.15 (8)	>7.7					
$Sc^{III}Br_4^-$	6.38 (8)	6.61 (8)	7.05 (8)	7.31 (8)	7.61 (8)		
$Mn^{II}Cl_3^-$		5.50 (6)	6.40 (8)	6.64 (8)	7.24 (8)	7.53 (8)	
$Mn^{II}Br_3^-$		5.36 (6)	5.92 (6)	6.08 (6)	6.53 (8)	6.92 (8)	7.24 (8)
$Fe^{II}Cl_3^-$	4.46 (8)	5.69 (8)	6.31 (8)	6.72 (8)	7.27 (8)	7.62 (8)	
$Fe^{II}Br_3^-$	4.42 (6)	5.43 (8)	5.85 (8)	6.09 (8)	6.62 (8)	7.18 (8)	7.37 (8)
$Co^{II}Cl_3^-$	4.9 (1)	5.78 (8)	6.34 (8)	6.65 (8)	7.21 (8)	7.61 (8)	
	5.27 (8)						
$Co^{II}Br_3^-$	4.8 (1)	~5.5	5.78 (8)	6.09 (8)	6.57 (8)	7.11 (8)	
	5.18 (8)						
$Ni^{II}Cl_3^-$	5.5 (1)	5.8 (1)	6.37 (8)	7.25 (8)	7.59 (8)		
$Ni^{II}Br_3^-$	5.1 (1)	~5.6	5.98 (8)	6.37 (8)	6.58 (8)	7.15 (8)	

[a]The numbers in parentheses represent the uncertainties in the last digit.

α-spin orbitals with Fe–X σ^* character. The lowest unoccupied MO (LUMO) is the d_{z^2} orbital from the Fe $3d$ β-spin orbitals.

B. MnX_3^- (X=Cl, Br) and the mix level scheme

The tri-coordinate d^5 $Mn^{II}X_3^-$ has a D_{3h} geometry. Electron detachment leads to a geometrical distortion from D_{3h} to a "T-shaped" C_{2v} structure for the neutral species, where one ∠X–Mn–X angle increases by about 20°. In the D_{3h} ligand field of MnX_3^-, the Mn $3d$ orbitals transform into e'', a_1', and e' with a slightly larger splitting energy than that in a T_d ligand field of a tetrahedral MnX_4^{2-} site. However, MnX_3^- still has a high-spin ground state because the halides are weak-field ligands. In a lower C_{2v} symmetry, these MOs transform as $e' \rightarrow (a_2, 1b_2)$, $a_1' \rightarrow 1a_1$, and $e'' \rightarrow (2a_1, b_1)$.[47] The spin exchange interaction of the metal center stabilizes the occupied α-spin orbitals relative to the β-spin orbitals. The spin splitting of the M^{II} site is smaller by 1.4–3.6 eV than that of the d^5 ferric site. Therefore, even though the Cl($3p$)/Br($4p$) orbitals in MnX_3^- lie below the $3d$ β-spin orbitals, some of the ligand orbitals are actually spaced in the same energy range as the $3d$ α-spin orbitals [Fig. 5(a)], resulting in the so-called "mixed level scheme."

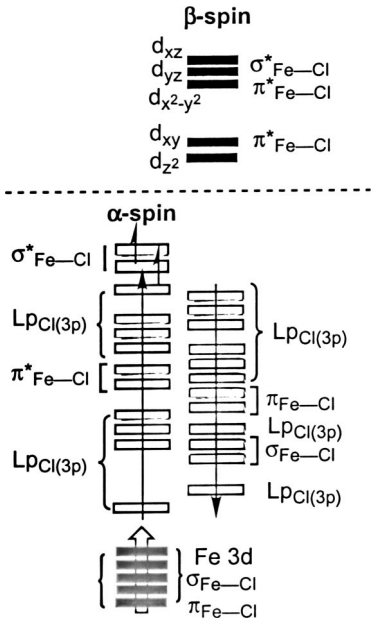

FIG. 4. Schematic molecular orbital diagram for $Fe^{III}Cl_4^-$. The Fermi level is indicated by a dashed line; the metal $3d$ orbitals and ligand orbitals are represented by the closed and open boxes, respectively. The arrows represent the closed spin orbitals.

C. FeX_3^-, CoX_3^-, and NiX_3^- (X=Cl, Br)

The mixed level scheme is pretty much kept for the tri-coordinate d^6 $Fe^{II}X_3^-$ and d^7 $Co^{II}X_3^-$ complexes; the additional $3d$ electrons are filled in the upper β-spin orbitals (Fig. 5). Since the extra electron enters an Fe d_{z^2} β-spin orbital in $Fe^{II}X_3^-$ with D_{3h} symmetry, the structure of the neutral $Fe^{III}X_3^0$, which is isoelectronic with MnX_3^-, remains D_{3h} symmetry. The HOMO of $Co^{II}X_3^-$ is either a Co d_{xy} β-spin orbital with Co–X σ^* character in a "T-shaped" C_{2v} structure or a Co d_{yz} β-spin orbital with Co–X π^* character in a slight "Y-shaped" C_{2v} structure (one ∠X–F–X angle is less than 120°). The latter is slightly more stable by 0.16 and 0.13 eV than the former for $Co^{II}Cl_3^-$ and $Co^{II}Br_3^-$, respectively. The oxidation of $Co^{II}X_3^-$ leads to a triangle d^6 complex $Co^{III}X_3^0$ with D_{3h} symmetry.

With the increasing atomic number, the energy levels of the metal-based orbitals decrease gradually relative to the ligand-based orbitals from MnX_3^- to NiX_3^- (Fig. 5). For the d^8 $Ni^{II}X_3^-$, the three occupied Ni $3d$ β-spin orbitals lie below the Cl($3p$)/Br($4p$) orbitals, quite different from the other three complexes. The HOMOs of $Ni^{II}X_3^-$ become the degenerate Cl($3p$) or near-degenerate Br($4p$) β-spin orbitals with Ni–X π^* character. The $Ni^{II}X_3^-$ complexes prefer a trigonal pyramidal structure with C_s symmetry. The neutral complexes NiX_3^0 upon electron detachment favor a quartet ground state, which is more stable by 0.28–0.44 eV than a doublet state of NiX_3^0. The neutral $NiCl_3$ species possesses a

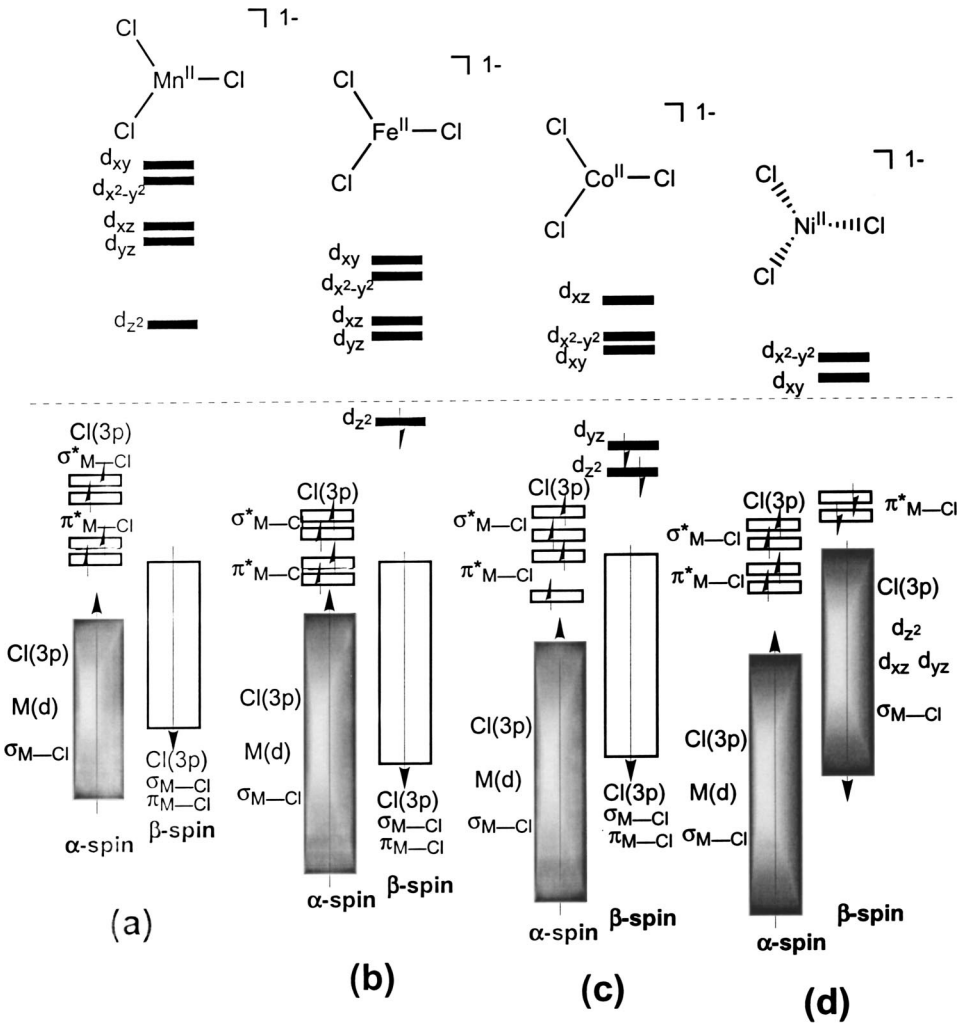

FIG. 5. Schematic molecular orbital diagrams for (a) $Mn^{II}Cl_3^-$, (b) $Fe^{II}Cl_3^-$, (c) $Co^{II}Cl_3^-$, and (d) $Ni^{II}Cl_3^-$. The Fermi level is indicated by a dashed line; the metal $3d$ orbitals and ligand orbitals are represented by the closed and open boxes, respectively; the mixing field of the metal $3d$ orbitals and ligand orbitals are represented by a gray box.

planar ''T-shaped'' structure with C_{2v} symmetry, while neutral $NiBr_3$ has a planar ''Y-shaped'' structure also with C_{2v} symmetry.

The B3LYP/6-311++G($3df$,$3pd$) optimized geometries of all the complex anions and their corresponding neutral are shown in Table III. The ADE and VDE of the threshold peak of each complex were also calculated and are compared to the experimental values in Table I.

V. SPECTRAL ASSIGNMENTS AND DISCUSSION

The PES features shown in Figs. 1–3 represent transitions from the ground state of the anions to the ground and excited states of the corresponding neutral molecules. Within the single-particle approximation, these PES features can be alternatively viewed as removing electrons from the occupied molecular orbitals of the anions. Our PES data revealed a very high density of electronic states for the metal halide complexes, due to the open *d*-shell and the spin–spin and spin–orbital couplings. A detailed state-by-state assignment for each spectrum is not feasible. We will qualitatively understand the PES spectra and compare with the theoretical results. It will be shown that the basic electronic features and trend of the $3d$ metal halide complexes as represented in Figs. 4 and 5 are consistent with our PES data.

A. FeX_4^- (X=Cl, Br)

The electron configuration of Sc in ScX_4^- is d^0 and its PES spectrum provides an excellent reference to distinguish between $3d$ and ligand features for the tetra-coordinate ferric complexes. The 157 nm spectrum of $ScCl_4^-$ [Fig. 1(c)] showed two strong features at a very high binding energies, which should be entirely due to detachment from ligand-based MOs. The overall two-band pattern in the spectrum of $FeCl_4^-$ is similar to that of the $ScCl_4^-$ spectrum and should be due to the ligands accordingly, although the *X* band of $FeCl_4^-$ is broad with resolved fine features. Due to the lower electron binding energy of Br^- relative to Cl^- and the stronger spin–orbit splitting in Br, the $ScBr_4^-$ spectrum [Fig. 1(d)] shifted to lower binding energies and exhibited many more features, which should all be due to detachment from the Br-based ligand orbitals. The spectral pattern of $FeBr_4^-$ is also similar to that of $ScBr_4^-$ except that the *X* band in $FeBr_4^-$ [Fig. 1(b)] is much broader and intense, analogous to that observed in $FeCl_4^-$ relative to $ScCl_4^-$.

Our observed PES pattern for $FeCl_4^-$ is consistent with the calculated MO diagram shown in Fig. 4, where the solid bars represent the MOs with mainly metal character while the hollow bars represent the MOs with primarily ligand character. The large stabilization of the Fe $3d$ α orbitals as a

TABLE III. The spin states and B3LYP/6-311++G($3df$,$3pd$) optimized structural parameters of MX_4^-, MX_3^-, and their corresponding neutrals.

	S	S^2	M X^a	M X^b	X^b M X^b	X^b M X^a
$FeCl_4^-$	5/2	8.76	2.231	2.231	109.5	109.5
$FeBr_4^-$	5/2	8.76	2.382	2.382	109.5	109.5
$MnCl_3^-$	5/2	8.76	2.308	2.308	120.0	120.0
$MnBr_3^-$	5/2	8.76	2.454	2.454	120.0	120.0
$FeCl_3^-$	2	6.01	2.242	2.242	120.0	120.0
$FeBr_3^-$	2	6.01	2.388	2.388	120.0	120.0
$CoCl_3^-$–T	3/2	3.76	2.234	2.233	132.0	113.9
$CoCl_3^-$–Y[c]	3/2	3.76	2.215	2.225	118.0	120.9
$CoBr_3^-$–T	3/2	3.76	2.376	2.374	130.8	114.6
$CoBr_3^-$–Y[c]	3/2	3.76	2.364	2.360	115.4	122.3
$Ni^{II}Cl_3^-$	1	2.01	2.193	2.195	119.0	118.5
$Ni^{II}Br_3^-$	1	2.01	2.344	2.333	110.0	124.9
$FeCl_4^0$	2	6.15	2.137	2.137	126.0	101.8
$FeBr_4^0$	2	6.23	2.298	2.298	123.5	102.9
$MnCl_3^0$	2	6.12	2.154	2.139	141.0	109.5
$MnBr_3^0$	2	6.21	2.310	2.305	139.8	110.1
$FeCl_3^0$	5/2	8.76	2.143	2.143	120.0	120.0
$FeBr_3^0$	5/2	8.76	2.287	2.287	120.0	120.0
$CoCl_3^0$	2	6.01	2.104	2.104	120.0	120.0
$CoBr_3^0$	2	6.01	2.284	2.284	120.0	120.0
$NiCl_3^0$–T[c]	3/2	3.76	2.109	2.086	123.2	118.4
$NiCl_3^0$–Y	3/2	3.76	2.115	2.115	120.0	120.0
$NiBr_3^0$	3/2	3.76	2.221	2.245	115.9	122.0

[a,b]Referred to C_{2v} or C_S $MX^a(X^b)_2$.
[c]The ground state.

result of the strong spin polarization pushed the $3d$ α orbitals below the ligand-based orbitals, giving rise to the ''inverted level scheme.'' The HOMO of the ferric $FeCl_4^-$ is the degenerate Cl($3p$) α-spin orbitals with a σ_{Fe-Cl} antibonding character. Thus, a better electron donor ligand will lead to lower electron binding energies, as observed in the spectrum of $FeBr_4^-$ relative to that of $FeCl_4^-$. The σ_{Fe-X} antibonding character of the HOMO of FeX_4^-, indicative of the covalent character between the Fe–X bonding, is consistent with the broad X band observed in their PES spectra.

PES of $FeCl_4^-$ in single crystal $CsFeCl_4$ had been studied previously at variable photon energies (25–150 eV).[14] Three broad peaks were observed in the PES spectra in the electron binding energy range of 2–8 eV and were assigned using the relative intensity changes in the photon energy dependent study. The threshold peak was shown to have covalent mixing characters between Fe $3d$ and Cl $3p$; the second peak was shown to have the greatest atomic Cl-like behavior; and the highest binding energy band was shown to contain more Fe $3d$ character. This previous work confirmed the inverted level scheme in the $FeCl_4^-$ center, as shown in Fig. 4. Our PES spectrum of gaseous $FeCl_4^-$ [Fig. 1(a)] is similar to the first two peaks observed for $FeCl_4^-$ in the $CsFeCl_4$ crystal, but at much higher resolution. The covalent character of the HOMO observed in our PES data is consistent with the previous PES study, as well as a previous study using ligand K-edge x-ray absorption spectroscopy,[48] which showed 86% total covalency in $FeCl_4^-$ or 21.5% per Fe^{III}–Cl bond.

B. MnX_3^- and FeX_3^- (X=Cl, Br)

The spectra of the tri-coordinate ferrous complexes FeX_3^- (Fig. 2) showed a weak band at about 4.2 eV for both the Cl and Br complexes, indicating that this band must be from a purely $3d$ orbital. The second band (A) is well separated from the X band and showed a significant dependence on the ligand type, shifting to a lower binding energy by about 0.26 eV in the Br complex (Table II). The higher binding energy features (B to E) of the two complexes also have clear resemblance and shifted to lower binding energies in the Br complex. These observations suggest that the higher binding energy features should be due to ligand-based MOs. These overall spectral patterns for the tri-coordinate ferrous complexes agree well with the calculated MO spectral pattern shown in Fig. 5(b) for $FeCl_3^-$. The calculated MO pattern revealed a ''mixed level scheme,'' in that the Fe $3d$ α orbitals are in the same energy region as the ligand orbitals, due to the smaller spin-polarization in the ferrous complexes. The X band is then due to detachment from the β electron in the d_{z^2} orbital [Fig. 5(b)]. The A band should come from detachment from the HOMO of the α-spin orbitals, which consist of ligand-based MOs with σ_{Fe-X} antibonding characters. The broad width of the A band is consistent with the Fe–X covalent character of these MOs. The higher binding energy features (B,C,…) are relatively sharp and should all be due to pure ligand-based MOs. However, in the PES spectra of the tri-coordinate ferrous complexes, we could not clearly identify detachment features from the $3d$ α orbitals, either because they have binding energies beyond our photon energies or they are mixed/buried in the features from ligand-based MOs due to their lower detachment cross sections.

The spectra of the MnX_3^- complexes are similar to those of FeX_3^-, except that the weak lower binding energy peak (X) present in the FeX_3^- spectra were missing. This observa-

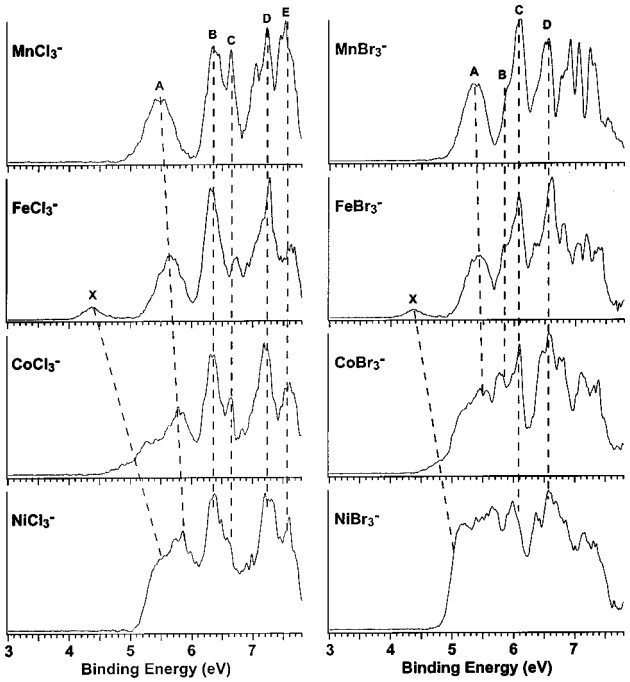

FIG. 6. Comparison of the 157 nm PES spectra of MX_3^- (M=Mn, Fe, Co, Ni; X=Cl, Br). The dashed lines are drawn to guide the eyes.

tion is consistent with the d^5 configuration of Mn^{II} and confirms that the extra electron in the ferrous complexes enters into the d_{z^2} HOMO in FeX_3^-, as revealed from the computed MO diagrams (Fig. 5). Therefore, the HOMO of MnX_3^- consists of the ligand α-spin orbitals, resulting in much higher and ligand-dependent ADEs and VDEs compared to the d^6 FeX_3^- complexes.

C. CoX_3^- and NiX_3^- (X=Cl, Br)

The PES spectral features of CoX_3^- and NiX_3^- were broader and more congested, in particular near the threshold region (Fig. 3). But the overall spectral patterns of the high binding energy regions are still quite similar to that of FeX_3^- and MnX_3^-, as compared in Fig. 6. The major difference among the spectra of CoX_3^-, NiX_3^-, and FeX_3^-, is the shift of the threshold band. The *A* band of $CoCl_3^-$ [Fig. 3(a)] still resembles that of $FeCl_3^-$. However, the threshold region of $CoCl_3^-$ showed two broad and weak features ($X1$ and $X2$), which were closely spaced to the *A* band, in contrast to the single and well-separated *X* band of FeX_3^-. These observations agree well with the calculated MOs [Fig. 5(c)], which shows two β-spin electrons in the d_{xy} and d_{z^2} HOMOs and the lower-lying ligand-based MOs are very similar to that of $FeCl_3^-$. The $X1$ and $X2$ threshold bands are due to detachment of the two β-spin electrons in the d_{xy} and d_{z^2} HOMOs, which have higher binding energies compared to the d_{z^2} β electron in $FeCl_3^-$, due to the increased nuclear charge of Co.

The spectra of NiX_3^- showed three major differences from the lighter $3d$ metal complexes: (1) more spectral congestion near the threshold region; (2) lack of weak low binding energy features present in the spectra of FeX_3^- and CoX_3^-; (3) the threshold peaks are intense and showed dependence on the ligand type, shifting to lower binding energies in the Br complex relative to that of the Cl complex. However, the high binding energy part of the NiX_3^- spectra is still similar to those of the lighter $3d$ metal complexes (Fig. 6). These observations suggest that the HOMO of the NiX_3^- complexes should be mainly ligand-based MOs. The spectral congestion near the threshold region may be caused by the overlap of the occupied $3d$ β-spin orbitals with the ligand-based MOs. These observations are consistent with the calculated MO level scheme, shown in Fig. 5(d) for $NiCl_3^-$. The $3d$ β electrons in the Ni complexes are stabilized so much that they are pulled down to the same energy region as the ligand-based MOs. The HOMO of NiX_3^- becomes the ligand-based β-spin orbitals with $\pi^*_{\mathrm{Ni-Cl}}$ character [Fig. 5(d)].

Figure 6 summarizes and compares the two series of metal complexes, MCl_3^- and MBr_3^-. Guided by the dashed lines, we can see that the threshold band due to detachment from the metal $3d$ β-spin orbitals shifts rapidly to higher binding energies from FeX_3^- to NiX_3^-. The *A* band in each spectrum also shows an obvious shift to higher binding energies, while the higher binding energy bands show almost no shift. Our calculations suggest that the highest occupied α-spin orbitals of all the MX_3^- complexes involve a degenerate ligand orbital with $\sigma^*_{\mathrm{M-X}}$ character. These MOs are responsible for the *A* band. The dependence of this band on the metal center and its broad width are consistent with the M–L covalency, similar to the HOMO of $FeCl_4^-$. The independence of the higher binding energy features in the spectra of MCl_3^- and MBr_3^- (Fig. 6) is consistent with their pure ligand characters.

D. The electronic structure of NiX_3^- and its potential implication for NiFe hydrogenase

Our experimental and theoretical results reveal that the electronic structure of NiX_3^- is unique among the series of $3d$ metal halides, i.e., the degenerate $Cl(3p)$ or near-degenerate $Br(4p)$ β-spin orbitals with Ni–X π^* character become the HOMOs of $Ni^{II}X_3^-$ and the $3d$ β electrons are stabilized and located below the ligand MOs. This suggests that oxidation of Ni^{2+} complexes with weak-field ligand (better electron donor), such as the halides, will involve oxidation of the ligand, instead of the metal ($Ni^{II} \rightarrow Ni^{III}$). In the active site of *Desulfovibrio gigas* NiFe hydrogenase, a Ni atom coordinates with four cysteine sulfur ligands and probably one oxo anion.[49] There are several oxidation forms of the enzyme, but x-ray absorption spectroscopy experiments indicated that the Ni center does not undergo major electron density changes through the catalytic cycle, as there are no significant shifts of the Ni absorption edge.[50] This observation is consistent with our results, suggesting that a ligand charge transfer process may be involved in the catalytic cycle of the NiFe hydrogenase.

E. ADEs and redox potentials

A one-electron oxidation reaction, aside from solvation effects, is similar to electron detachment in the gas phase.

Therefore, the gas phase ADEs should be inherently related to oxidation potentials, except that the solvation effects are absent in the electron detachment in vacuum. As discussed earlier, the threshold feature *X* in the PES spectrum of Fe or Co complex corresponds to removing a β spin $3d$ electron from the HOMO of each species. This detachment process represents an oxidation of M(II)→M(III) (M=Fe, Co). As we have shown previously,[30,32] the width of the redox feature of $[Fe(SCH_3)_4]^-$, i.e., the energy difference between the VDE and ADE of the feature (*X*), directly reflects the geometry changes after one electron is transferred, and hence is related to the intrinsic reorganization energy upon oxidization (λ_{ox}). The VDE and ADE differences of all the complexes are listed in Table I. The large values of λ_{ox} for the d^5 complexes FeX_4^- and MnX_3^- suggest big geometry changes for the oxidation of these systems and are confirmed by our calculations.

VI. CONCLUSIONS

Photoelectron spectroscopy and DFT calculations on a series of transition metal halide complexes: $Fe^{III}X_4^-$ and $M^{II}X_3^-$ (M=Mn, Fe, Co, Ni, X=Cl, Br) are reported. Electronic structures of these complexes and their trend with the ligand-field geometry and metal center substitution are investigated. Photoelectron spectra of the tetrahedrally coordinated ferric complexes $Fe^{III}X_4^-$ (X=Cl, Br) were obtained at 157 nm. All the spectral features were assigned to detachment from ligand orbitals by comparing with the spectra of the d^0 complexes, $Sc^{III}X_4^-$ (X=Cl, Br), and confirmed their ''inverted level scheme'' electronic structures. Photoelectron spectra of the series of tri-coordinate $3d$ transition metal halides $M^{II}X_3^-$ (M=Mn, Fe, Co, Ni, X=Cl, Br) were taken at 193 and 157 nm. The spectral features show strong ligand and photon energy dependence. Spin polarizations driven by the spin–exchange interaction are also revealed by the calculations, but the MO diagrams exhibit a ''mixed level scheme'' for these tri-coordinate complexes, in which the ligand-based MOs and the $3d$ majority spin orbitals are spaced closely in the same energy regions. The DFT results show that the energies of the metal-based orbitals decrease gradually relative to the ligand-based orbitals from Mn to Ni for MX_3^- and agree very well with the observed PES spectra.

ACKNOWLEDGMENTS

Support by the National Institutes of Health (GM-63555 to L.S.W. and GM45303 to T.I.) is gratefully acknowledged. The experimental work and some of the calculations were performed using the molecular science computing facility at the W. R. Wiley Environmental Molecular Sciences Laboratory, a national scientific user facility sponsored by DOE's Office of Biological and Environmental Research and located at Pacific Northwest National Laboratory, which is operated for DOE by Battelle.

[1] R. A. Bair and W. A. Goddard III, J. Am. Chem. Soc. **100**, 5669 (1978).
[2] J. B. Koernera and T. Ichiye, J. Phys. Chem. B **101**, 3633 (1997).
[3] D. J. Vaughan, J. A. Tossell, and K. H. Johnson, Geochim. Cosmochim. Acta **38**, 993 (1974).
[4] J. G. Noman, Jr. and S. C. Jachels, J. Am. Chem. Soc. **97**, 3833 (1975).
[5] L. Noodleman, J. G. Norman, Jr., J. H. Osborne, A. Aizman, and D. A. Case, J. Am. Chem. Soc. **107**, 3418 (1985).
[6] L. Noodelman and D. A. Case, Adv. Inorg. Chem. **38**, 423 (1992).
[7] L. Noodelman, C. Y. Peng, D. A. Case, and J. M. Mouesca, Coord. Chem. Rev. **144**, 199 (1995).
[8] B. W. Beck, J. B. Koerner, and T. Ichiye, J. Phys. Chem. B **103**, 8006 (1999).
[9] R. W. Lane, J. A. Ibers, R. B. Frankel, G. C. Papaefthymious, and R. H. Holm, J. Am. Chem. Soc. **99**, 84 (1977).
[10] M. R. Churchill and J. Wormald, Inorg. Chem. **14**, 2657 (1975).
[11] D. Coucouvanis, D. Swenson, N. C. Baenziger, D. G. Holah, A. Kostikas, A. Simopoulos, and V. Petrouleas, J. Am. Chem. Soc. **98**, 5721 (1976).
[12] M. S. Gebhard, J. C. Deaton, S. A. Koch, M. Millar, and E. I. Solomon, J. Am. Chem. Soc. **112**, 2217 (1990).
[13] M. S. Gebhard, S. A. Koch, M. Millar, F. J. Devlin, P. J. Stephens, and E. I. Solomon, J. Am. Chem. Soc. **113**, 1640 (1991).
[14] K. D. Butcher, S. V. Didziulis, B. Briat, and E. I. Solomon, J. Am. Chem. Soc. **112**, 2231 (1990).
[15] K. D. Butcher, S. V. Didziulis, B. Briat, and E. I. Solomon, Inorg. Chem. **29**, 1626 (1990).
[16] K. D. Butcher, M. S. Gebhard, and E. I. Solomon, Inorg. Chem. **29**, 2607 (1990).
[17] K. Rose Williams, B. Hedman, K. O. Hodgson, and E. I. Solomon, Inorg. Chim. Acta **263**, 315 (1997).
[18] K. Rose, S. E. Shadle, M. K. Eidsness, D. M. Kurtz, Jr., R. A. Scott, B. Hedman, K. O. Hodgson, and E. I. Solomon, J. Am. Chem. Soc. **120**, 10743 (1998).
[19] J. B. Howard and D. C. Rees, Chem. Rev. (Washington, D.C.) **96**, 2965 (1996).
[20] O. Einsle, F. A. Tezcan, S. L. A. Andrade, B. Schmid, M. Yoshida, J. B. Howard, and D. C. Rees, Science **297**, 1696 (2002).
[21] H. I. Lee, B. J. Hales, and B. M. Hoffman, J. Am. Chem. Soc. **119**, 11395 (1997).
[22] S. J. Yoo, H. C. Angove, V. Papaefthymiou, B. K. Burgess, and E. J. Münck, J. Am. Chem. Soc. **122**, 4926 (2000).
[23] F. M. MacDonnell, K. Ruhlandt-Senge, J. J. Ellison, R. H. Holm, and P. P. Power, Inorg. Chem. **34**, 1815 (1995).
[24] Y. Sanakis, P. P. Power, A. Stubna, and E. Münk, Inorg. Chem. **41**, 2690 (2002).
[25] A. Hanspeter, E. L. Boninaar, J. M. Smith, N. A. Eckert, P. L. Hollard, and E. Münk, J. Am. Chem. Soc. **124**, 3012 (2002).
[26] L. S. Wang, C. F. Ding, X. B. Wang, and S. E. Barlow, Rev. Sci. Instrum. **70**, 1957 (1999).
[27] L. S. Wang and X. B. Wang, J. Phys. Chem. A **104**, 1978 (2000).
[28] X. B. Wang, L. S. Wang, R. Brown, P. Schwerdtfeger, D. Schroder, and H. Schwarz, J. Chem. Phys. **114**, 7388 (2001).
[29] X. B. Wang and L. S. Wang, J. Phys. Chem. A **104**, 4429 (2000).
[30] X. B. Wang and L. S. Wang, J. Chem. Phys. **112**, 6959 (2000).
[31] X. B. Wang and L. S. Wang, J. Am. Chem. Soc. **122**, 2096 (2000); **122**, 2339 (2000).
[32] X. Yang, X. B. Wang, Y. J. Fu, and L. S. Wang, J. Phys. Chem. A **107**, 1703 (2003).
[33] S. Q. Niu, X. B. Wang, J. A. Nichols, L. S. Wang, and T. Ichiye, J. Phys. Chem. A **107**, 2898 (2003).
[34] X. B. Wang and L. S. Wang, Phys. Rev. Lett. **83**, 3402 (1999).
[35] R. G. Parr and W. Yang, *Density-Functional Theory of Atoms and Molecules* (Oxford University Press, Oxford, 1989).
[36] A. D. Becke, Phys. Rev. A **38**, 3098 (1988).
[37] A. D. Becke, J. Chem. Phys. **98**, 1372 (1993); **98**, 5648 (1993).
[38] C. Lee, W. Yang, and R. G. Parr, Phys. Rev. B **37**, 785 (1988).
[39] S. Q. Niu, J. A. Nichols and T. Ichiye, J. Phys. Chem. B (submitted).
[40] A. J. H. Wachters, J. Chem. Phys. **52**, 1033 (1970).
[41] P. J. Hay, J. Chem. Phys. **66**, 4377 (1977).
[42] K. Raghavachari and G. W. Trucks, J. Chem. Phys. **91**, 1062 (1989).
[43] R. Stowasser and R. Hoffmann, J. Am. Chem. Soc. **121**, 3414 (1999).
[44] R. J. Harrison, J. A. Nichols, T. P. Straatsma *et al.*, NWChem, A Computational Chemistry Package for Parallel Computers, Version 4.1, 2002, Pacific Northwest National Laboratory, Richland, WA 99352-0999.
[45] G. Black, J. Chase, B. Didier *et al.*, Ecce, A Problem Solving Environ-

ment for Computational Chemistry, Software Version 3.0, 2002, Pacific Northwest National Laboratory, Richland, WA 99352-0999.
[46] G. L. Gutsev and A. I. Boldyrev, Chem. Phys. **56**, 277 (1981).
[47] T. A. Albright, J. K. Burdett, and M. H. Whangbo, *Orbital Interactions in Chemistry* (Wiley, New York, 1985).
[48] S. E. Shadle, B. Hedman, K. O. Hodgson, and E. I. Solomon, J. Am. Chem. Soc. **117**, 2259 (1995).
[49] A. Volbeda, M. H. Charon, C. Piras, E. C. Hatchikian, M. Frey, and J. C. Fontecilla-Camps, Nature (London) **373**, 580 (1995).
[50] Z. Gu, J. Dong, C. B. Allan *et al.*, J. Am. Chem. Soc. **118**, 11155 (1996).